J. Fluid Mech. (2022), *vol*. 943, A39, doi:10.1017/jfm.2022.458

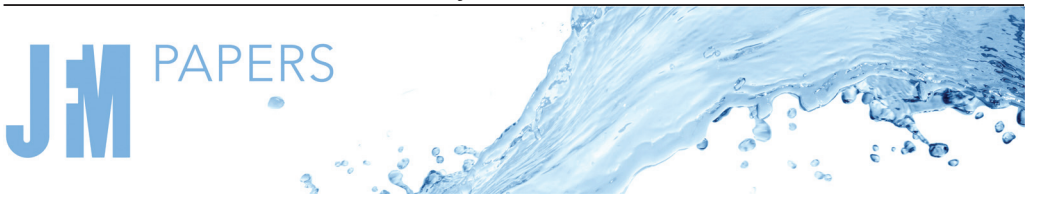

Theoretical analysis of close-contact melting on superhydrophobic surfaces

Yoram Kozak†

School of Mechanical Engineering, Tel Aviv University, Tel Aviv 69978, Israel

(Received 23 August 2021; revised 14 March 2022; accepted 12 May 2022)

The present study deals with close-contact melting of a vertical cylinder on a horizontal isothermal superhydrophobic surface with an array of circular posts. A new numerical model for this phenomenon is formulated under several simplifying assumptions. For the limiting case of perfect slip and thermal contact, based on the model assumptions, it is demonstrated that superhydrophobic surfaces can enhance the melting time by no more than 30 %. Numerical solution of the new model reveals that the effect of superhydrophobic hydrodynamic slip can decrease the molten layer thickness. However, due to the dominant effect of thermal slip, the heat transfer rate can be decreased significantly, and the melting time can be roughly doubled. An approximate analytical model is developed for understanding the problem dynamics better. The analytical model predictions are compared extensively against the numerical model results. For sufficiently low surface volume fractions, the analytical model provides excellent estimations of the numerical model predictions. Dimensional analysis reveals that according to the analytical model, the ratio between the melting times for superhydrophobic and regular surfaces is governed by a single dimensionless group. Moreover, according to the analytical model, the melting time on a superhydrophobic surface is always longer than on a regular surface, which agrees qualitatively with the numerical model results. Based on this analysis, a dimensionless condition for the analytical model range of validity is formulated. Finally, a conservative criterion for the liquid–gas interface stability under a close-contact melting process is established.

Key words: solidification/melting

† Email address for correspondence: kozaky@tauex.tau.ac.il

1. Introduction

Close-contact melting is observed commonly in daily life when butter is melted in a hot pan. Almost instantly, a thin liquid layer is formed between the melting butter and the hot pan surface. Then heat is conducted through the thin layer and the melt is squeezed continuously to the sides by the butter's weight. This special type of melting is actually encountered in various industrial and engineering applications. For instance, it is essential for development of heated drilling devices that can bore into ice by close-contact melting (Shreve 1962; Schüller & Kowalski 2017; Park *et al.* 2021), as well as design of platforms designated for standing on melting ice sheets (Lea & Stegall 1973). Other examples include analysing lubrication characteristics of moving sliders (Wilson 1976), and even development of self-burying nuclear reactors that can melt their way into the Earth's core once overheated (Emerman & Turcotte 1983). Note that in a regular melting process, a thick liquid layer grows continuously between the hot surface and the melting solid. This liquid layer creates a thermal resistance that decreases the heat transfer rate over time. On the other hand, the liquid layer formed in a close-contact melting process typically remains thin (< 1 mm) (Ziskind & Kozak 2018). Thus the heat transfer rates are significantly higher in comparison with a regular melting process. In fact, it was demonstrated that by initiating close-contact melting in finned latent heat thermal energy storage units, the melting rate can be enhanced by 2.5 times, in comparison with a regular melting process (Kozak, Rozenfeld & Ziskind 2014).

The above-mentioned possible applications have driven fundamental research of close-contact melting phenomena for various basic configurations. The first simple configuration examined was melting in a spherical shell, which was initially studied experimentally and theoretically (Moore & Bayazitoglu 1982), and then improved modelling capabilities were developed (Bahrami & Wang 1987). The similar problem of close-contact melting in horizontal cylindrical capsules was also explored experimentally (Sparrow & Geiger 1986) as well as analytically (Bareiss & Beer 1984). Further extensions of this model for an elliptical capsule were developed later (Fomin, Wilchinsky & Saitoh 2000). The dynamics of close-contact melting in a heated annulus was explored both experimentally and theoretically (Betzel & Beer 1988). An extensive analysis for close-contact melting in a rectangular enclosure with different aspect ratios and phase change materials was also performed (Hirata, Makino & Kaneko 1991). The problem of hot cylindrical (Moallemi & Viskanta 1986) and spherical (Emerman & Turcotte 1983) bodies that melt through an infinite solid medium was also addressed. Finally, different physical effects for close-contact melting of rectangular blocks on heated surfaces were studied, such as sliding (Groulx & Lacroix 2006) and unsteady melting (Myers, Mitchell & Muchatibaya 2008). For such simple configurations, the melting rate and molten layer thickness can usually be predicted via analytical models based on thin-layer approximation and other simplifying assumptions (Bejan 1992, 1994). One fundamental configuration that was explored extensively is close-contact melting of a vertical cylinder on a horizontal isothermal surface. Early works dealt with experimental and theoretical analysis of a vertical cylinder pressed by an external force on a hot horizontal surface (Saito *et al.* 1985*a*, *b*). The influence of material type, surface temperature, applied force and cylinder dimensions was determined. The same case without external forcing was later investigated experimentally and theoretically (Moallemi, Webb & Viskanta 1986). It was shown that an analytical model can be derived for the melt fraction under simplifying assumptions. The influence of more complex effects, such as the inclusion of nanoparticles (Hu *et al.* 2018) and non-Newtonian viscoplastic properties (Kozak *et al.* 2019), was also addressed recently. The similar case of an isothermal vertical cylindrical capsule has also been

investigated (Saito *et al.* 1986; Chen *et al.* 1993). Note that accurate prediction of the melting process in this case is much more involved due to interaction between natural convection in the melt and solid bulk motion. A full solution of this problem has been achieved only recently (Shockner & Ziskind 2021), as it requires specially designed numerical methods (see, for instance, Gudibande & Iyer 2017; Kasibhatla *et al.* 2017; Kozak & Ziskind 2017; Faden *et al.* 2018; Pan *et al.* 2018; Kasibhatla & Brüggemann 2021.

It has been demonstrated in the past that the hot surface structure can influence significantly the close-contact melting process. Saito, Hong & Hirokane (1992) proved, both experimentally and theoretically, that the heat transfer rate can be enhanced by slitting radial grooves in the surface. This configuration reduces the pressure in the molten layer leading to a thinner layer that creates a lower thermal resistance and higher heat transfer rates. Turkyilmazoglu (2019) also demonstrated that the close-contact melting dynamics can be altered by using a permeable surface. Today, it is possible to design and fabricate micro-textured surfaces with remarkable properties (Ybert *et al.* 2007). In particular, the surface roughness allows the liquid contact angle to exceed 150°, yielding a non-wetting superhydrophobic surface (Chen, Guo & Liu 2017). Two superhydrophobic states can be achieved: the Wenzel and Cassie states (Lafuma & Quéré 2003). For the Wenzel case, the liquid is impregnated inside the surface texture. On the other hand, for the Cassie case, gas pockets remain trapped in the surface texture, and a stable liquid–gas interface is established on the surface. Transition between Cassie and Wenzel states is also possible (Zheng, Yu & Zhao 2005; Patankar 2010; Papadopoulos *et al.* 2013). For instance, the liquid–gas interface can collapse under high pressure conditions and wet the surface texture, leading to a Cassie–Wenzel transition (Xue *et al.* 2012, 2016; Emami *et al.* 2013; Hemeda & Tafreshi Vahedi 2014; Lv *et al.* 2014; Fang *et al.* 2018).

In recent years, superhydrophobic surfaces in the Cassie state have shown great promise for various applications, such as drag reduction (Lauga & Stone 2003; Ou, Perot & Rothstein 2004; Liravi *et al.* 2020), enhanced condensation heat transfer (Miljkovic, Enright & Wang 2013), anti-icing (Hejazi, Sobolev & Nosonovsky 2013) and thermal insulation (Shao, Wang & Bai 2020). However, the phenomenon of close-contact melting on superhydrophobic surfaces has not been investigated either experimentally or theoretically. It is known that superhydrophobic surfaces in the Cassie state induce partial hydrodynamic slip, due to the trapped gas pockets (Rothstein 2010). Drag is reduced as gases are typically less viscous than liquids (Lee, Choi & Kim 2016). Potentially, superhydrophobic surfaces can reduce the pressure in the thin molten layer, which is governed by viscous forces (Ockendon & Ockendon 1995). As a result, the molten layer thickness can decrease and the heat transfer rate can be enhanced, similarly to the approach suggested by Saito *et al.* (1992). Nevertheless, superhydrophobic surfaces also induce thermal slip, due to imperfect thermal contact between the solid surface and the liquid layer (Enright *et al.* 2014; Steigerwalt Lam *et al.* 2014). This effect can impede the heat transfer rates. A recent study by Aljaghtham, Premnath & Alsulami (2021) addressed this interplay between hydrodynamic and thermal slips for close-contact melting of a rectangular block under the influence of a magnetic field. The slip effects were modelled via Navier boundary conditions with arbitrary chosen slip lengths. It was found that the effect of hydrodynamic slip alone increases the melting rate, whereas the inclusion of thermal slip decreases the melting rate. Nevertheless, the dynamics of this interplay for close-contact melting on a superhydrophobic surface with a certain micro-texture, temperature and melting material is unclear. Also, the conditions for a stable liquid–gas interface that retains the Cassie state under a close-contact melting process are unknown currently.

In the current work, we present, for the first time, a detailed derivation of a numerical model for close-contact melting of a vertical cylinder on a horizontal isothermal superhydrophobic surface with an array of circular posts. Predictions of the melt fraction, molten layer thickness and heat transfer rate, for a representative case of an ice cylinder, are shown. An approximate analytical model is derived as well, and its range of validity is investigated. Finally, a conservative criterion for the liquid–gas interface stability under close-contact melting conditions is established.

2. Theoretical model formulation

The general schematics of the numerical model that will be developed in this section are shown in figure 1. Figure 1(*a*) presents an isometric view of a superhydrophobic surface with an equidistant array of circular posts, where h denotes the post height. The top view of this surface is presented in figure 1(*b*), where d is the post diameter, and l is the distance between two posts. Figure 1(*c*) presents the physical problem, close-contact melting of an ice cylinder on an isothermal superhydrophobic surface. The cylinder has initial radius and height R and H, respectively, whereas the upper surface position is denoted by s. Also, the r and z coordinate system used for the model formulation is shown. A thin molten layer with thickness δ is formed between the ice and the hot surface. Due to gravity g, the melt in the layer is squeezed to the sides by the ice cylinder's own weight. Figure 1(*d*) shows representative examples of the resulting velocity and temperature profiles, u and T, in the thin molten layer. The surface and ice melting temperatures, T_w and T_m, respectively, are presented, as well as the hydrodynamic and thermal slip lengths, λ and λ_t, respectively.

The model is based on the following assumptions: (*a*) thin-layer approximation, hence the molten layer thickness is much smaller than the cylinder's dimensions; (*b*) the upper ice interface shape remains flat; (*c*) sensible heating effects are negligible; (*d*) the flow in the thin molten layer is laminar; (*e*) the ice motion as well as the flow and heat transfer in the thin molten layer are quasi-steady; (*f*) the effect of convection in the melt is negligible; (*g*) material properties are constant; (*h*) pressure gradients in the z-direction are negligible; (*i*) the solid surface is perfectly isothermal; (*j*) heat transfer through the gas layers is negligible; (*k*) the substrate pattern effect can be modelled via an effective slip length. Note that assumptions (*a*)–(*h*) are typical for close-contact melting problems and were validated experimentally for different configurations (Bareiss & Beer 1984; Moallemi & Viskanta 1986; Bejan 1994). Although some of these assumptions can be relaxed (see, for instance, Yoo, Hong & Kim 1998; Groulx & Lacroix 2003, 2007; Cregan, Williams & Myers 2020), the contribution of these additional physical effects on the melting rate is usually not significant for low Stefan and high Prandtl numbers. Assumptions (*i*) and (*j*) are valid only for sufficiently high ratios between the solid surface and gas thermal conductivities. Assumption (*k*) indicates that the alternating slip/no-slip boundary condition induced by the substrate pattern can be modelled via boundary condition homogenization. As the description of wetting hydrodynamics requires a microscopic model to avoid contact line singularity, the Navier slip boundary condition with an appropriate slip length is utilized; see Snoeijer & Andreotti (2013) for a detailed discussion.

The range of validity of assumptions (*i*) and (*j*) can be estimated by the analysis presented below. The thermal resistances of the solid and gas layers, R_s and R_g, respectively, are

$$R_s = \frac{h}{k_s \phi}, \quad R_g = \frac{h}{k_g (1-\phi)}, \tag{2.1a,b}$$

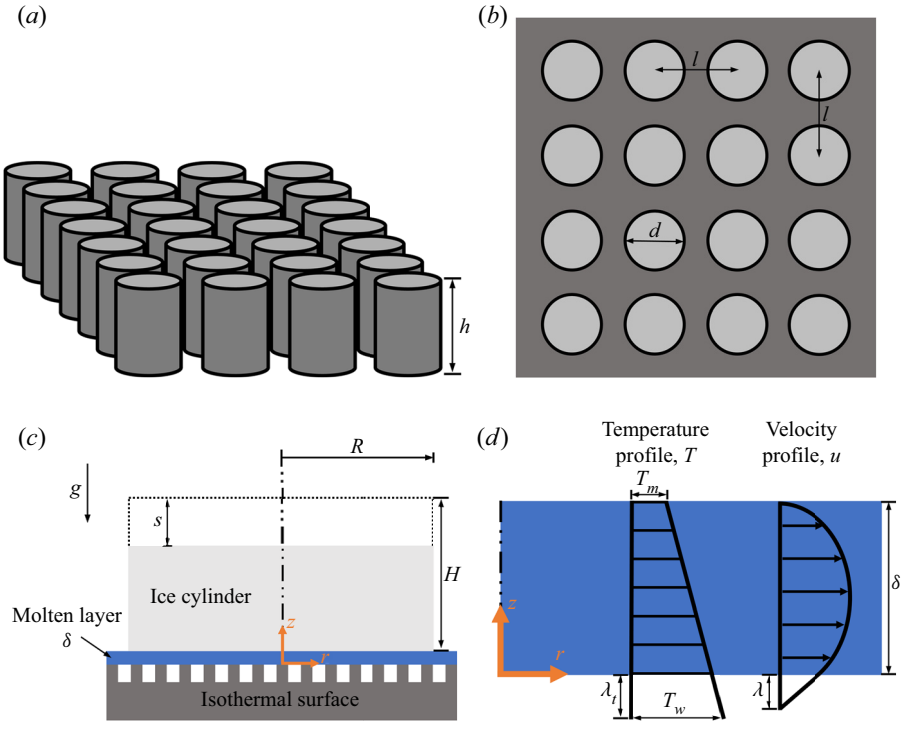

Figure 1. General schematics of the numerical model. (*a*) Isometric view of a superhydrophobic surface with an equidistant array of circular posts. (*b*) Top view of the surface. (*c*) Close-contact melting of an ice cylinder on an isothermal superhydrophobic surface. (*d*) The flow and heat transfer in the thin molten layer.

where h is the post height, k_s and k_g are the solid surface and gas thermal conductivities, respectively, and ϕ is the solid surface volume fraction, which is given by the following analytical expression for the considered geometry:

$$\phi = \frac{\pi d^2}{4l^2}. \tag{2.2}$$

Assumption (*i*) is valid as long as the thermal resistance of the solid layer is sufficiently small. A criterion for estimating this assumption validity can be formulated as

$$T_w - T_m \gg \Delta T = q'' R_s, \tag{2.3}$$

where q'' is the heat flux, and ΔT is the temperature difference across the solid layer, i.e. the temperature difference between the base and the top of each post. Equation (2.3) states that the temperature difference between the surface and the melting point is much greater than the temperature difference across the solid surface. Thus the temperature difference across the solid surface can be considered negligible. Equation (2.1*a*,*b*) can be substituted into (2.3) yielding the condition

$$k_s \gg \frac{q'' h}{(T_w - T_m)\phi}, \tag{2.4}$$

For typical values $q'' = 10^5\,\mathrm{W\,m^{-2}}$, $h = 10\,\mu\mathrm{m}$, $T_w - T_m = 10\,\mathrm{K}$ and $\phi = 0.01$, (2.4) yields $k_s \gg 10\,\mathrm{W\,mK^{-1}}$, which is applicable for several possible solid surface materials.

Assumption (*j*) is valid as long as the gas layer thermal resistance is significantly higher than the solid layer thermal resistance:

$$R_g \gg R_s. \tag{2.5}$$

Substitution of (2.1*a*,*b*) into (2.5) yields

$$\frac{k_s}{k_g} \gg \frac{1-\phi}{\phi}. \tag{2.6}$$

For a relatively low value of $\phi = 0.01$, (2.6) provides approximately the condition $k_s/k_g \gg 100$. This condition holds for many solid and gas material combinations. However, it is clear that the analysis above indicates that assumptions (*i*) and (*j*) are not valid in general.

It is important to stress that ϕ is also connected to the wall wettability, according to Quéré (2008):

$$\cos\theta^* = (1-\phi)\cos\theta - 1, \tag{2.7}$$

where θ and θ^* are the contact angle and the apparent contact angle, respectively. Thus for low values of ϕ, the surface wettability decreases as the apparent contact angle increases. Also, although the micro-structure pattern has no cylindrical symmetry, according to assumption (*k*), a homogeneous Navier slip boundary can be applied for the macro-scale cylindrical symmetric flow. This assumption is valid as the substrate micro-structure pattern is smaller by several orders of magnitude in comparison with the macro-scale flow.

Following assumptions (*a*)–(*k*), a numerical model for close-contact melting on isothermal superhydrophobic surfaces can be formulated. The model will be able to predict the resulting melting rate, molten layer thickness and heat transfer rate for given conditions. First, the momentum equation for the *r*-direction velocity component under thin-layer approximation (see assumption (*a*)) is invoked:

$$\frac{\partial p}{\partial r} = \mu \frac{\partial^2 u_r}{\partial z^2}, \tag{2.8}$$

where p is pressure, μ is dynamic viscosity, and u_r is the *r*-direction velocity component. Equation (2.8) can be integrated twice with respect to z to derive an expression for the radial velocity profile:

$$u_r(z) = \frac{1}{2\mu}\frac{\partial p}{\partial r} z^2 + C_1 z + C_2, \tag{2.9}$$

where C_1 and C_2 are integration constants. Two boundary conditions are applied for finding the integration constants values: the Navier boundary condition (Rothstein 2010) for partial slip at the superhydrophobic surface ($z = 0$), and the no-slip condition at the solid ice surface ($z = \delta$):

$$u_r(z=0) = \lambda \frac{\partial u_r}{\partial z}(z=0), \tag{2.10}$$

$$u_r(z=\delta) = 0, \tag{2.11}$$

where λ is the hydrodynamic slip length (Davis & Lauga 2010). The integration constants C_1 and C_2 can be determined by substituting (2.9) into (2.10) and (2.11):

$$C_1 = -\frac{1}{2\mu(\lambda+\delta)}\frac{\partial p}{\partial r}\delta^2, \tag{2.12}$$

$$C_2 = -\frac{\lambda}{2\mu(\lambda+\delta)}\frac{\partial p}{\partial r}\delta^2. \tag{2.13}$$

The following expression for the r-direction velocity profile in the thin molten layer can be found by substituting (2.12) and (2.13) back into (2.9):

$$u_r(z) = \frac{1}{2\mu}\frac{\partial p}{\partial r}\left(z^2 - \frac{\delta^2}{\lambda+\delta}[z+\lambda]\right). \tag{2.14}$$

The two-dimensional radial continuity equation is invoked for finding the pressure distribution in the thin molten layer:

$$\frac{1}{r}\frac{\partial}{\partial r}(ru_r) + \frac{\partial u_z}{\partial z} = 0, \tag{2.15}$$

where u_z is the z-direction velocity component. Equation (2.15) can be integrated with respect to z across the thin molten layer:

$$\int_0^\delta \frac{1}{r}\frac{\partial}{\partial r}(ru_r)\,\mathrm{d}z + u_z(z=\delta) - u_z(z=0) = 0. \tag{2.16}$$

Two boundary conditions can be applied: a no-penetration condition at the superhydrophobic surface ($z = 0$), and the solid velocity at the ice surface ($z = \delta$):

$$u_z(z=0) = 0, \tag{2.17}$$

$$u_z(z=\delta) = -\frac{\mathrm{d}s}{\mathrm{d}t}, \tag{2.18}$$

where s is the upper solid surface position and t is time. By substituting (2.14), (2.17) and (2.18) into (2.16), the following expression can be derived:

$$\int_0^\delta \frac{1}{r}\frac{\partial}{\partial r}\left(r\frac{1}{2\mu}\frac{\partial p}{\partial r}\left(z^2 - \frac{\delta^2}{\lambda+\delta}[z+\lambda]\right)\right)\mathrm{d}z - \frac{\mathrm{d}s}{\mathrm{d}t} = 0. \tag{2.19}$$

Integration of (2.19) yields the following differential equation for the pressure distribution:

$$\frac{1}{r}\frac{\partial}{\partial r}\left(r\frac{\partial p}{\partial r}\right) = -\frac{12\mu}{\delta^3}\frac{\mathrm{d}s}{\mathrm{d}t}\frac{\delta+\lambda}{\delta+4\lambda}. \tag{2.20}$$

An explicit expression for the pressure can be derived by integrating (2.20) twice with respect to r:

$$p(r) = -\frac{3\mu}{\delta^3}\frac{\mathrm{d}s}{\mathrm{d}t}\frac{\delta+\lambda}{\delta+4\lambda}r^2 + C_3\ln(r) + C_4, \tag{2.21}$$

where C_3 and C_4 are integration constants. The integration constants can be found via two boundary conditions: zero pressure gradient at the cylinder's centre ($r = 0$), and zero

gauge pressure at the thin molten layer outlet ($r = R$):

$$\frac{\partial p}{\partial r}(r = 0) = 0, \tag{2.22}$$

$$p(r = R) = 0. \tag{2.23}$$

The integration constants C_3 and C_4 are determined by substituting (2.21) into (2.22) and (2.23):

$$C_3 = 0, \tag{2.24}$$

$$C_4 = \frac{3\mu}{\delta^3}\frac{\mathrm{d}s}{\mathrm{d}t}\frac{\delta + \lambda}{\delta + 4\lambda}R^2. \tag{2.25}$$

The pressure distribution in the thin molten layer can be derived by substituting (2.24) and (2.25) back into (2.21):

$$p(r) = \frac{3\mu}{\delta^3}\frac{\mathrm{d}s}{\mathrm{d}t}\frac{\delta + \lambda}{\delta + 4\lambda}(R^2 - r^2). \tag{2.26}$$

The heat transfer equation in the thin molten layer, under assumptions (*e*) and (*f*), is invoked for finding the solid velocity:

$$\frac{\partial^2 T}{\partial z^2} = 0, \tag{2.27}$$

where T is temperature. Equation (2.27) can be integrated twice with respect to z, yielding the expression

$$T(z) = C_5 z + C_6, \tag{2.28}$$

where C_5 and C_6 are integration constants. The integration constants are determined via two boundary conditions: thermal slip (Steigerwalt Lam *et al.* 2014) at the superhydrophobic surface ($z = 0$), and melting point temperature at the ice surface ($z = \delta$):

$$T_w - T(z = 0) = -\lambda_t \frac{\partial T}{\partial z}(z = 0), \tag{2.29}$$

$$T(z = \delta) = T_m, \tag{2.30}$$

where T_w and T_m are the wall and melting point temperatures, respectively, and λ_t is the thermal slip length (Enright *et al.* 2014). By substituting (2.28) into (2.29) and (2.30), the integration constants C_5 and C_6 can be determined:

$$C_5 = \frac{T_m - T_w}{\delta + \lambda_t}, \tag{2.31}$$

$$C_6 = T_w + \lambda_t \frac{T_m - T_w}{\delta + \lambda_t}. \tag{2.32}$$

The temperature distribution in the thin molten layer can be found by substituting (2.31) and (2.32) back into (2.28):

$$T(z) = T_w + \frac{T_m - T_w}{\delta + \lambda_t}(z + \lambda_t). \tag{2.33}$$

The Stefan condition (Alexiades & Solomon 2018), under assumption (*c*), can be utilized for coupling the heating rate and the solid interface velocity:

$$\rho_s L \frac{\mathrm{d}s}{\mathrm{d}t} = -k \frac{\mathrm{d}T}{\mathrm{d}z}(z = \delta), \tag{2.34}$$

where ρ_s is the solid phase density, L is latent heat of fusion per unit mass, and k is the liquid phase thermal conductivity. The solid velocity can be found by substituting (2.33) into (2.34):

$$\frac{\mathrm{d}s}{\mathrm{d}t} = \frac{k}{\rho_s L} \frac{T_w - T_m}{\delta + \lambda_t}. \tag{2.35}$$

An explicit relation between the pressure distribution and the molten layer thickness can now be derived by substituting (2.35) into (2.26):

$$p(r) = \frac{3\mu}{\delta^3} \frac{k}{\rho_s L} \frac{T_w - T_m}{\delta + \lambda_t} \frac{\delta + \lambda}{\delta + 4\lambda} (R^2 - r^2). \tag{2.36}$$

The force balance between the pressure forces and the solid weight, under assumption (*e*), is invoked for finding a relation between the molten layer thickness and the solid upper interface position:

$$\int_0^R 2\pi r\, p(r)\, \mathrm{d}r = g\rho_s \pi R^2 (H - s), \tag{2.37}$$

where H is the ice cylinder's initial height, and g is the gravitational acceleration. Equation (2.36) can be substituted into (2.37), and after integration, the following relation can be derived:

$$\frac{3}{2} \frac{\mu R^2}{\delta^3} \frac{k}{\rho_s L} \frac{T_w - T_m}{\delta + \lambda_t} \frac{\delta + \lambda}{\delta + 4\lambda} = g\rho_s (H - s). \tag{2.38}$$

Equations (2.35) and (2.38) comprise a set of first-order ordinary differential and nonlinear algebraic equations, respectively, that can be solved numerically for the solid melting rate and molten layer thickness. For the model closure, a relation for the hydrodynamic and thermal slip lengths should be provided. For the hydrodynamic slip length, we will utilize a simple theoretical expression from Davis & Lauga (2010) for a superhydrophobic surface with circular posts, which is applicable for $\phi < 0.2$:

$$\frac{\lambda}{l} = \frac{3}{16}\sqrt{\frac{\pi}{\phi}} - \frac{3}{2\pi} \ln(1 + \sqrt{2}), \tag{2.39}$$

where l is the distance between two posts, and ϕ is the solid volume fraction of the surface material. The thermal slip length can be derived by the following expression from Enright *et al.* (2014) that relates the hydrodynamic and thermal slip lengths:

$$\lambda = \tfrac{3}{4}\lambda_t. \tag{2.40}$$

Substituting (2.39) into (2.40) yields the following expression for the thermal slip length:

$$\frac{\lambda_t}{l} = \frac{1}{4}\sqrt{\frac{\pi}{\phi}} - \frac{2}{\pi} \ln(1 + \sqrt{2}). \tag{2.41}$$

Note that the distance between two posts, l, depends on the post diameter d and the solid volume fraction ϕ via the relation (Hemeda & Tafreshi Vahedi 2014)

$$l = \sqrt{\frac{\pi d^2}{4\phi}}. \tag{2.42}$$

3. Limiting case – perfect slip and thermal contact

It is of interest to investigate a limiting case that offers an analytical solution for (2.35) and (2.38). In particular, the case of perfect hydrodynamic slip and thermal contact (constant surface temperature) will reveal the maximum possible theoretical enhancement in the melting rate by a superhydrophobic surface. It is clear that existing superhydrophobic surfaces always induce both hydrodynamic and thermal slip. Nevertheless, it is of interest to understand the role of reduced thermal slip, as in the future, different techniques for reducing thermal slip, while still maintaining high hydrodynamic slip, can be introduced. Therefore, the maximum possible enhancement in the melting time by superhydrophobic surfaces can be used to determine the practical usefulness of thermal slip reduction. This case corresponds to the limits $\lambda \to \infty$ and $\lambda_t \to 0$. It is also equivalent for replacing (2.10) and (2.29) with perfect slip and constant surface temperature conditions, respectively. Under this limiting case, (2.38) is simplified to the form

$$\frac{3}{8}\frac{\mu R^2}{\delta^4}\frac{k(T_w - T_m)}{\rho_s L} = g\rho_s(H - s). \tag{3.1}$$

The molten layer thickness δ can now be isolated:

$$\delta = \left[\frac{3}{8}\frac{\mu R^2}{g\rho_s(H - s)}\frac{k(T_w - T_m)}{\rho_s L}\right]^{1/4}. \tag{3.2}$$

Equation (3.2) can be substituted into (2.35) under the limit $\lambda_t \to 0$ to yield the ordinary differential equation

$$\frac{\mathrm{d}s}{\mathrm{d}t} = \left(\frac{3}{8}\frac{\mu R^2}{g\rho_s}\right)^{-1/4}\left(\frac{k(T_w - T_m)}{\rho_s L}\right)^{3/4}(H - s)^{1/4}. \tag{3.3}$$

Equation (3.3) can be solved analytically via variable separation and integration:

$$\int_0^s \frac{\mathrm{d}s}{(H - s)^{1/4}} = \left(\frac{3}{8}\frac{\mu R^2}{g\rho_s}\right)^{-1/4}\left(\frac{k(T_w - T_m)}{\rho_s L}\right)^{3/4}\int_0^t \mathrm{d}t. \tag{3.4}$$

Integration of (3.4) yields an analytical solution for the solid upper interface position as a function of time:

$$s = H - \left[H^{3/4} - \left(\frac{3}{8}\frac{\mu R^2}{g\rho_s}\right)^{-1/4}\left(\frac{k(T_w - T_m)}{\rho_s L}\right)^{3/4} t\right]^{4/3}. \tag{3.5}$$

The total melting time is the time when the solid upper interface reaches the surface, and it can be found by substituting $s = H$ into (3.5):

$$t_{melt}^{slip} = \frac{4}{3}H^{3/4}\left(\frac{3}{8}\frac{\mu R^2}{g\rho_s}\right)^{1/4}\left(\frac{k(T_w - T_m)}{\rho_s L}\right)^{-3/4}. \tag{3.6}$$

Note that the classical analytical solution with a no-slip boundary condition at the hot isothermal surface by Moallemi *et al.* (1986) predicts the following melting time, under

Property	Symbol	Value	Units
Liquid thermal conductivity	k	0.56	$\mathrm{W\,mK^{-1}}$
Latent heat of fusion	L	334×10^3	$\mathrm{J\,kg^{-1}}$
Solid density	ρ_s	916	$\mathrm{kg\,m^{-3}}$
Melting point	T_m	273.15	K
Dynamic viscosity	μ	1.8×10^{-3}	$\mathrm{kg\,ms^{-1}}$
Gravitational acceleration	g	9.81	$\mathrm{m\,s^{-2}}$

Table 1. Material properties and parameter values.

the same conditions:

$$t_{melt}^{no\text{-}slip} = \frac{4}{3} H^{3/4} \left(\frac{3}{2} \frac{\mu R^2}{g \rho_s} \right)^{1/4} \left(\frac{k(T_w - T_m)}{\rho_s L} \right)^{-3/4}. \tag{3.7}$$

The ratio between (3.6) and (3.7) provides an analytical relation for the maximum possible enhancement in the melting time by using a superhydrophobic surface:

$$t_{melt}^{slip} / t_{melt}^{no\text{-}slip} = 1/\sqrt{2} \approx 70\,\%, \tag{3.8}$$

Equation (3.8) reveals that for perfect hydrodynamic slip and thermal contact, it is possible theoretically to decrease the melting time by about 30 % in comparison with a regular isothermal surface with a no-slip boundary condition.

4. Numerical model solution method

The model governing equations (2.35) and (2.38) do not admit an analytical solution and must be solved numerically. Equation (2.35) can be discretized by a simple forward Euler scheme:

$$s^{n+1} = s^n + \frac{k}{\rho_s L} \frac{T_w - T_m}{\delta^n + \lambda_t} \Delta t, \tag{4.1}$$

where n and $n+1$ denote the current and next time steps, respectively, and Δt is discrete time step. The nonlinear algebraic equation (2.38) can be solved in a coupled manner with (4.1) via the scheme

$$\frac{3}{2} \frac{\mu R^2}{(\delta^n)^3} \frac{k}{\rho_s L} \frac{T_w - T_m}{\delta^n + \lambda_t} \frac{\delta^n + \lambda}{\delta^n + 4\lambda} = g \rho_s (H - s^n). \tag{4.2}$$

Also, the following initial condition, which states that the initial upper solid interface position is zero, is applied:

$$s(t = 0) = 0. \tag{4.3}$$

For each time step, (4.2) is solved for δ^n via a nonlinear algebraic equation solver. Then the new interface position, s^{n+1}, is calculated via (4.1). Note that the hydrodynamic and thermal slip lengths, λ and λ_t, are calculated via (2.39) and (2.41), respectively. For the first time step, $s^n = 0$ according to (4.3). The material properties of ice and water that are utilized in the current study, as well as relevant parameter values, can be found in table 1. Also, a time step $\Delta t = 10^{-3}$ s was found to be sufficiently small for proper convergence of all the tested cases.

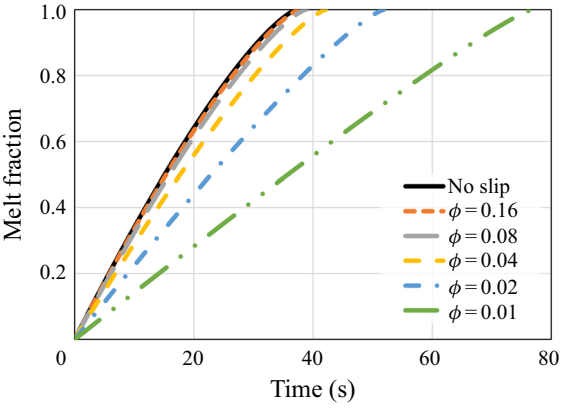

Figure 2. The melt fraction as a function of time according to the predictions of the numerical model and the classical no-slip constant wall temperature analytical solution (5.1). Different values of the surface solid volume fraction ϕ are examined.

5. Numerical model results and discussion

The predictions of the numerical model, which was formulated in § 2, are presented and discussed in the current section. The model is explored for a representative case with wall temperature $T_w = 293.15$ K, cylinder height and radius $H = R = 1$ cm, and post diameter $d = 6\,\mu$m, whereas the distance between two posts, l, can be determined according to (2.42). The chosen values correspond to realistic close-contact melting on regular surfaces experiments (Saito *et al.* 1985*a*; Moallemi *et al.* 1986) and superhydrophobic surface geometry from the literature (Lobaton & Salamon 2007), which was utilized for other applications. Note that the micro-structure substrate pattern was found to impact significantly the surface wettability and slip length (Ou *et al.* 2004). This is in accordance with different theoretical predictions; see Lobaton & Salamon (2007) and Davis & Lauga (2010). The effect of the surface solid volume fraction ϕ, for values 0.16, 0.08, 0.04, 0.02 and 0.01, is explored. The results are compared against the classical analytical solution for a regular isothermal surface with a no-slip boundary condition by Moallemi *et al.* (1986):

$$s_{no\text{-}slip} = H - \left[H^{3/4} - \left(\frac{3}{2} \frac{\mu R^2}{g \rho_s} \right)^{-1/4} \left(\frac{k(T_w - T_m)}{\rho_s L} \right)^{3/4} t \right]^{4/3}. \tag{5.1}$$

First, the melt fraction, which equals s/H, as a function of time is presented in figure 2. The results demonstrate that for relatively high ϕ values, the melting progression is only slightly slower than the no-slip perfect thermal contact case. However, for lower values of ϕ, the melting time increases much more significantly, whereas for the lowest value, $\phi = 0.01$, the total melting time is roughly doubled. The results reveal that the thermal slip has a much more dominant effect than the hydrodynamic slip on the melting rate as the melting time increases monotonically with the decrease of ϕ.

The dynamics of the melting process is explored further in figure 3, which presents the molten layer thickness, δ, as a function of time, for all the same cases. The analytical solution for the molten layer thickness under no-slip and constant surface temperature

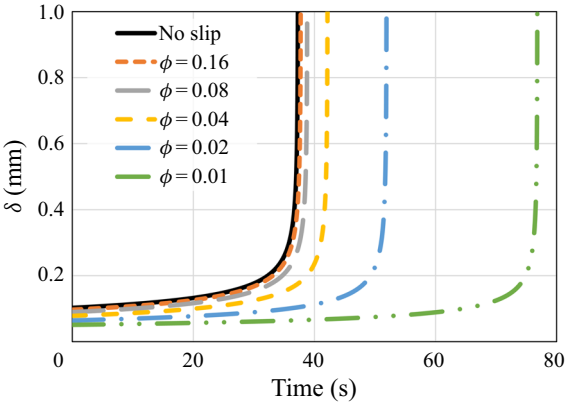

Figure 3. The molten layer thickness δ as a function of time according to the predictions of the numerical model and the classical no-slip constant wall temperature analytical solution (5.2). Different values of the surface solid volume fraction ϕ are examined.

conditions is

$$\delta_{no\text{-}slip} = \left(\frac{3}{2} \frac{k(T_w - T_m)\mu R^2}{g\rho_s^2 L(H - s_{no\text{-}slip})} \right)^{1/4}. \tag{5.2}$$

In a manner similar to the results presented in figure 2, for relatively high values of ϕ, the molten layer thickness is only slightly decreased in comparison with the classical no-slip analytical solution. Also, for lower values of ϕ, the molten layer thickness is reduced significantly in a monotonic trend due to the hydrodynamic slip. Although this reduction should decrease the molten layer thermal resistance and thus increase the melting rate, the thermal slip creates an additional, much higher, thermal resistance that increases the melting time. It is stressed that the rapid increase in the molten layer thickness at the end of the melting process is due to the very low remaining solid mass. It is clear that once the molten layer thickness is sufficiently large, the assumption of a thin molten layer does not hold. Nevertheless, this situation occurs only after most of the solid material has melted and thus does not affect significantly the overall melting process.

In addition, these resulting trends are investigated by calculating the heat flux at the surface via the right-hand side of the Stefan condition (see (2.34)):

$$q'' = k \frac{T_w - T_m}{\delta + \lambda_t}. \tag{5.3}$$

The heat flux for a no-slip constant temperature surface can be derived by the analytical expression

$$q''_{no\text{-}slip} = \left(\frac{2}{3} \frac{k^3 (T_w - T_m)^3 g\rho_s^2 L(H - s_{no\text{-}slip})}{\mu R^2} \right)^{1/4}. \tag{5.4}$$

Figure 4 shows the numerical model and the analytical solution results for the heat flux. In general, the heat flux decreases monotonically as ϕ decreases. Yet a very slight decrease in the heat flux in comparison with the no-slip analytical solution is observed for relatively high values of ϕ. For lower values of ϕ, the decrease in the heat flux is much more substantial. For $\phi = 0.01$, the reduction at $t = 0$ s is more than two times in

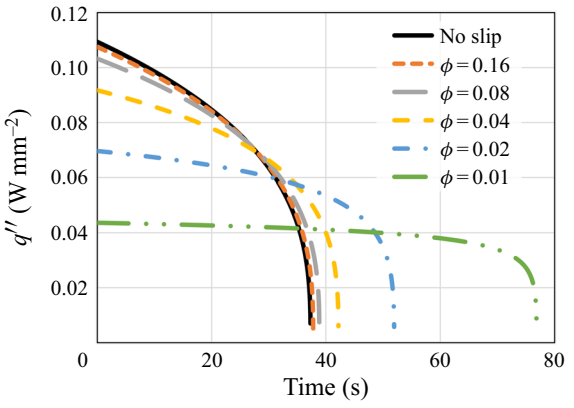

Figure 4. The heat flux q'' as a function of time according to the predictions of the numerical model and the classical no-slip constant surface temperature analytical solution (5.4). Different values of the surface solid volume fraction ϕ are examined.

comparison with a regular no-slip surface. According to (5.3), it is clear that as k, T_w and T_m are constants, and the molten layer thickness δ is lower than the no-slip case (see figure 3), the lower heat flux must be a result of high values of thermal slip length λ_t.

6. Approximate analytical model

The numerical model developed in the previous sections provides an accurate solution of the problem governing equations. However, it is of interest to develop an approximate analytical model that will reveal some of the basic features of the problem and provide quick estimations. Two approximate assumptions can be applied to achieve this goal: (1) $\lambda \approx \lambda_t$; (2) $4\lambda \gg \delta$. It is worth noting that assumption (1) leads to a constant error of 33 % in the hydrodynamic slip length (see (2.40)), and assumption (2) can never hold at the final stages of the melting as $\delta \to \infty$ (see figure 3). Nevertheless, it will be demonstrated that under certain conditions, the predictions of an analytical approximate model, which is governed by assumptions (1) and (2), can provide excellent agreement with the numerical model results.

Under assumptions (1) and (2), (2.38) can be reduced into the form

$$\frac{3}{8}\frac{\mu R^2}{\delta^3}\frac{k}{\rho_s L}\frac{T_w - T_m}{\lambda_t} = g\rho_s(H - s). \tag{6.1}$$

Equation (6.1) allows us to isolate the molten layer thickness δ:

$$\delta = \left(\frac{3}{8}\frac{\mu R^2}{g\rho_s^2(H - s)}\frac{k}{L}\frac{T_w - T_m}{\lambda_t}\right)^{1/3}. \tag{6.2}$$

Also, an explicit expression for the heat flux q'' can be obtained by substituting (6.2) into (5.3):

$$q'' = k\frac{T_w - T_m}{\left(\frac{3}{8}\frac{\mu R^2}{g\rho_s^2(H - s)}\frac{k}{L}\frac{T_w - T_m}{\lambda_t}\right)^{1/3} + \lambda_t}. \tag{6.3}$$

Both (6.2) and (6.3) depend on the time-dependent upper solid interface position s. An explicit relation between s and time can be found by substituting (6.2) into (2.35) and applying integration:

$$\int_0^s \left[\left(\frac{3}{8} \frac{\mu R^2}{g\rho_s^2 (H-s)} \frac{k}{L} \frac{T_w - T_m}{\lambda_t} \right)^{1/3} + \lambda_t \right] \mathrm{d}s = k \frac{T_w - T_m}{\rho_s L} \int_0^t \mathrm{d}t. \tag{6.4}$$

The resulting solution of (6.4) provides the following analytical relation between the upper interface position s and time t:

$$\frac{3}{2} \left(\frac{3}{8} \frac{\mu R^2}{g\rho_s^2} \frac{k}{L} \frac{T_w - T_m}{\lambda_t} \right)^{1/3} \left(H^{2/3} - (H-s)^{2/3} \right) + \lambda_t s = k \frac{T_w - T_m}{\rho_s L} t. \tag{6.5}$$

The predictions derived by the analytical approximate model are compared against the numerical model results to determine the analytical model applicability and general trends. Figures 5(*a–e*) present the melt fraction as a function of time, for both the analytical and numerical models, for the same ϕ values and conditions as presented in § 4. In general, the analytical model overpredicts the total melting time, and the discrepancy between the analytical and numerical model is significant for relatively high values of ϕ; see figures 5(*a*,*b*). However, the analytical model provides better predictions as the value of ϕ decreases (see figure 5*c*), and for low ϕ values, the agreement between the analytical and numerical models is excellent (see figures 5*d*,*e*). It is worth noting that the trends of the melting time with the decrease of ϕ are very different between the two models. For the numerical model, the melting time increases monotonically as ϕ decreases. Yet for the analytical model, the trend is non-monotonic. As ϕ decreases, the melting time decreases; see figures 5(*a*,*b*,*c*). Then as ϕ decreases further, the melting time increases; see figures 5(*d*,*e*). These non-monotonic trends are attributed to assumption (2). For high ϕ values, the slip length is small, thus δ cannot be considered negligible in comparison with 4λ. As a result, the slip length continues to affect the solution even for very low slip length values. Thus the solution does not converge to the classical no-slip solution for low slip length values, which leads to a non-physical trend for the melting time.

The predictions of the molten layer thickness δ as a function of time are also compared between the analytical and numerical models under the same conditions; see figures 6(*a–e*). The analytical model overpredicts the molten layer thickness, and the discrepancy between the two models is significant for $\phi = 0.16$ and $\phi = 0.08$; see figures 6(*a*,*b*). However, as the value of ϕ decreases, the predictions improve (see figure 6*c*) and provide excellent estimation for low ϕ values (see figures 6*d*,*e*). Opposed to the melt fraction predictions, both the numerical and analytical models show the same trends – the molten layer thickness decreases as ϕ decreases.

Further comparison between the two models involves the predicted heat flux; see figures 7(*a–e*). The heat flux is underpredicted by the analytical model, and the agreement improves as ϕ decreases; see figures 7(*a*,*b*,*c*). For sufficiently low ϕ values, the two models provide almost indistinguishable results; see figures 7(*d*,*e*). The trends predicted by the two models differ. For the numerical model, the heat flux is decreasing monotonically with the decrease in ϕ, whereas for the analytical model, as ϕ decreases, the heat flux increases (see figures 7*a*,*b*,*c*) and then decreases (see figures 7*d*,*e*).

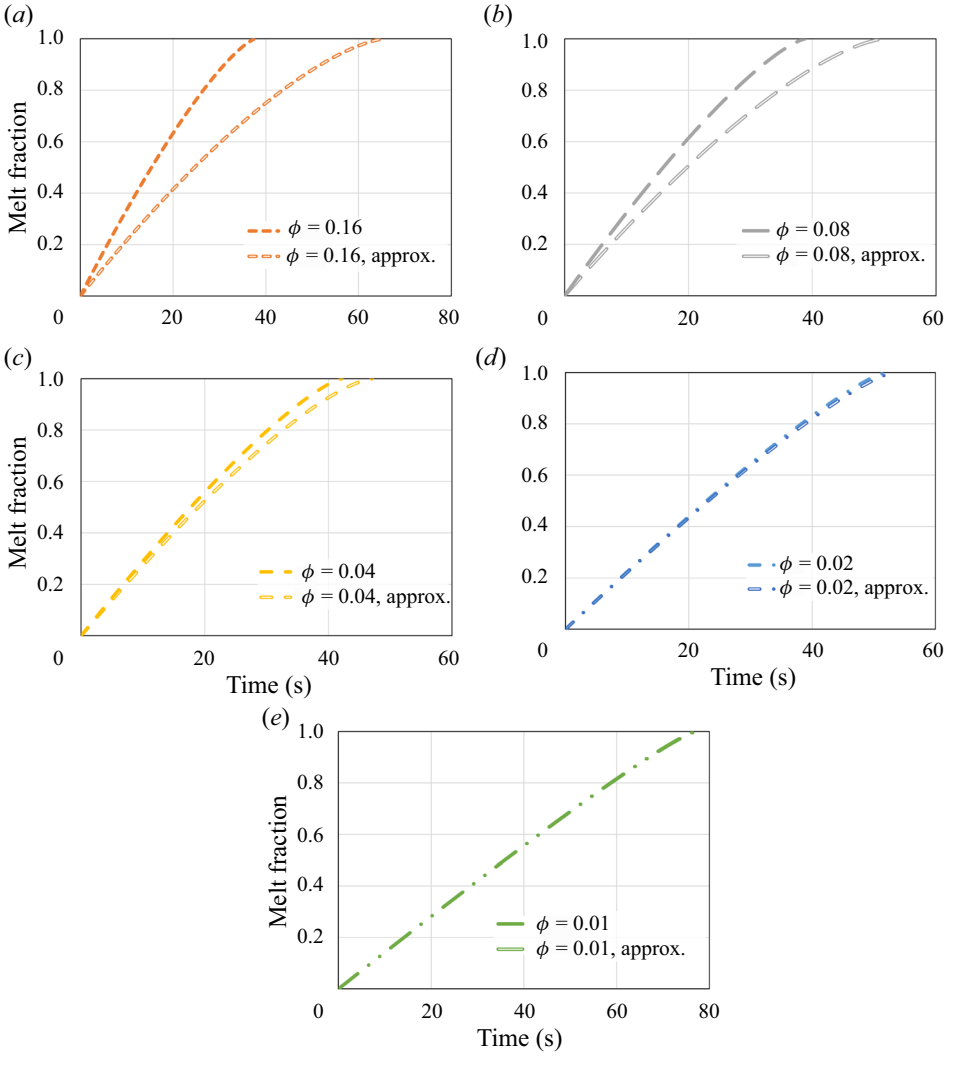

Figure 5. The melt fraction as a function of time – comparison between the numerical and approximate analytical models for: (*a*) $\phi = 0.16$, (*b*) $\phi = 0.08$, (*c*) $\phi = 0.04$, (*d*) $\phi = 0.02$, (*e*) $\phi = 0.01$.

The approximate analytical model can also provide a formula for the total melting time, t_{melt}, by substituting $s = H$ into (6.5):

$$t_{melt} = \frac{3}{2} H^{2/3} \left(\frac{3}{8} \frac{\mu R^2}{g \rho_s \lambda_t} \right)^{1/3} \left(k \frac{T_w - T_m}{L \rho_s} \right)^{-2/3} + \lambda_t H \left(k \frac{T_w - T_m}{L \rho_s} \right)^{-1}. \tag{6.6}$$

The analytical relation presented in (6.6) can be used for deriving an expression for the ratio of the melting times between isothermal superhydrophobic and regular surfaces (see also (3.7)):

$$\frac{t_{melt}}{t_{melt}^{no\text{-}slip}} = \left(\frac{3}{2} \right)^{-1/4} \frac{3}{4} \left[\frac{3}{4} 3^{1/3} \left(\frac{\mu R^2}{g H \lambda_t^4} k \frac{T_w - T_m}{L \rho_s^2} \right)^{1/12} + \left(\frac{\mu R^2}{g H \lambda_t^4} k \frac{T_w - T_m}{L \rho_s^2} \right)^{-1/4} \right]. \tag{6.7}$$

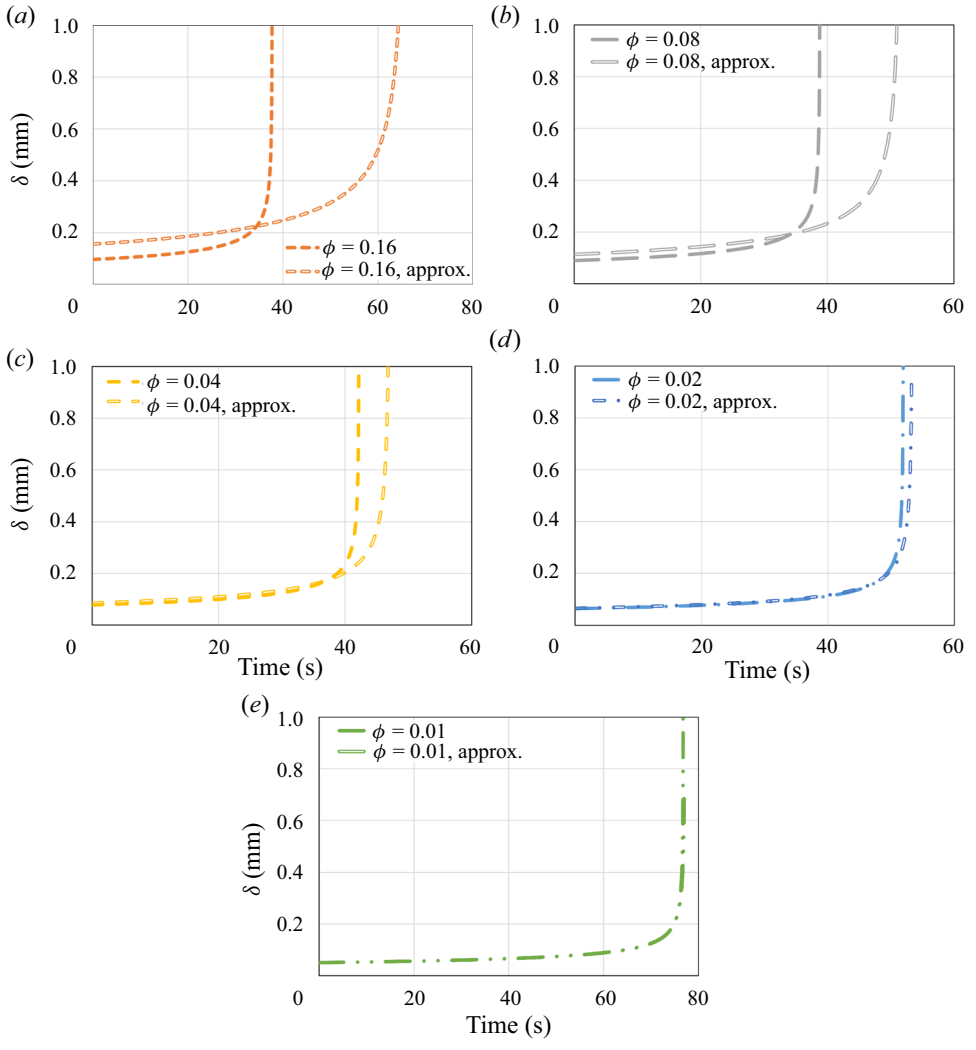

Figure 6. The molten layer thickness δ as a function of time – comparison between the numerical and approximate analytical models for: (*a*) $\phi = 0.16$, (*b*) $\phi = 0.08$, (*c*) $\phi = 0.04$, (*d*) $\phi = 0.02$, (*e*) $\phi = 0.01$.

Equation (6.7) reveals that the melting times ratio depends on a single dimensionless group that is denoted here as ε, where

$$\varepsilon = \frac{\mu R^2}{gH\lambda_t^4}\, k\, \frac{T_w - T_m}{L\rho_s^2}. \tag{6.8}$$

Substitution of (6.8) into (6.7) yields the following expression, which is a function of only ε:

$$\frac{t_{melt}}{t_{melt}^{no\text{-}slip}} = f(\varepsilon) = \left(\frac{3}{2}\right)^{-1/4} \frac{3}{4}\left[\frac{3}{4}\, 3^{1/3}\varepsilon^{1/12} + \varepsilon^{-1/4}\right]. \tag{6.9}$$

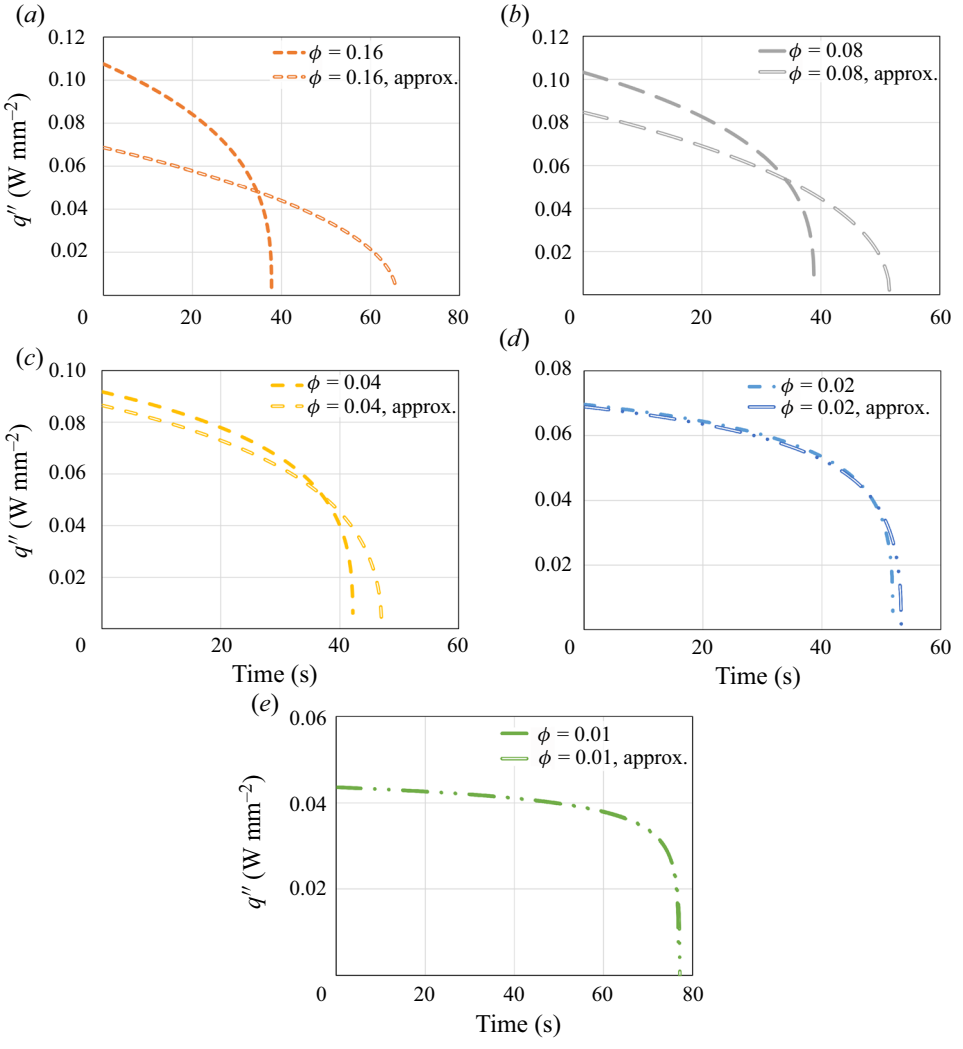

Figure 7. The heat flux q'' as a function of time – comparison between the numerical and approximate analytical models for: (*a*) $\phi = 0.16$, (*b*) $\phi = 0.08$, (*c*) $\phi = 0.04$, (*d*) $\phi = 0.02$, (*e*) $\phi = 0.01$.

Equation (6.9) can be differentiated with respect to ε and equated to zero to find an extremum point:

$$\frac{\mathrm{d}f(\varepsilon)}{\mathrm{d}\varepsilon} = \left(\frac{3}{2}\right)^{-1/4} \frac{3}{16}\left[\frac{3^{1/3}}{4}\varepsilon^{-11/12} - \varepsilon^{-5/4}\right] = 0. \tag{6.10}$$

Solution of (6.10) yields ε_{ext}, the ε value at the extremum point:

$$\varepsilon_{ext} = \frac{64}{3}. \tag{6.11}$$

Equation (6.10) can be differentiated again with respect to ε to find whether the extremum point is a maximum or minimum:

$$\frac{\mathrm{d}^2 f(\varepsilon)}{\mathrm{d}\varepsilon^2} = \left(\frac{3}{2}\right)^{-1/4} \frac{3}{64}\left[-\frac{11}{12}\, 3^{1/3}\varepsilon^{-23/12} + 5\varepsilon^{-9/4}\right]. \tag{6.12}$$

Substitution of (6.11) into (6.12) yields a positive value, thus the point is minimum. Substitution of (6.11) into (6.9) finds the minimum ratio between the melting times of superhydrophobic and regular surfaces:

$$\left(\frac{t_{melt}}{t_{melt}^{no\text{-}slip}}\right)_{min} \approx 1.26. \tag{6.13}$$

The analysis shows that the analytical model predicts that the melting time for a superhydrophobic surface will be greater by at least 26 % than a regular surface with no-slip and constant temperature boundary conditions. These results agree qualitatively with the numerical model predictions that showed that the melting time for superhydrophobic surfaces tends to increase. In order to investigate further the analytical model fundamental features, dimensional analysis is applied. The following dimensionless groups govern the problem:

$$\left.\begin{gathered} Ste = \frac{c_p(T_w - T_m)}{L}, \quad Ga = \frac{gH^3}{\nu^2}, \quad Pr = \frac{c_p\mu}{k}, \quad \rho_* = \frac{\rho_s}{\rho_l}, \\ s_* = \frac{s}{H}, \quad R_* = \frac{R}{H}, \quad \lambda_* = \frac{\lambda_t}{H}, \quad Fo = \frac{\alpha_l t}{H^2}, \end{gathered}\right\} \tag{6.14}$$

where Ste is the Stefan number, Ga is the Galilei number, Pr is the Prandtl number, ρ_* is the solid–liquid density ratio, s_* is the melt fraction, R_* is dimensionless radius, λ_* is dimensionless slip length, Fo is the Fourier number, c_p is specific heat, ν is kinematic viscosity, ρ_l is the liquid phase density, and α_l is the liquid phase thermal diffusivity. Based on this analysis, (6.8) can be rendered into dimensionless form:

$$\varepsilon = \frac{Ste\, R_*^2}{Ga\, Pr\, \rho_*^2 \lambda_*^4}. \tag{6.15}$$

Equations (6.2) and (6.3) can also be rendered into dimensionless form:

$$\frac{\delta}{H} = \delta_* = \lambda_* \left(\frac{3}{8}\frac{\varepsilon}{1 - s_*}\right)^{1/3}, \tag{6.16}$$

$$\frac{q''}{T_w - T_m}\frac{H}{k} = Nu = \lambda_*^{-1}\left[\left(\frac{3}{8}\frac{\varepsilon}{1 - s_*}\right)^{1/3} + 1\right]^{-1}, \tag{6.17}$$

where δ_* is the dimensionless molten layer thickness, and Nu is the Nusselt number. The analytical solution reveals that both δ_* and Nu depend on the dimensionless groups ε, s_* and λ_*. Equation (6.5) can also be rendered into dimensionless form:

$$\frac{Ste\, Fo}{\lambda_* \rho_*} = \frac{3}{2}\left(\frac{3}{8}\varepsilon\right)^{1/3}(1 - (1 - s_*)^{2/3}) + s_*. \tag{6.18}$$

Although an explicit expression for s_* cannot be derived, it is clear that s_* depends on two dimensionless groups: $Ste\, Fo/\rho_*\lambda_*$ and ε. An expression for the dimensionless

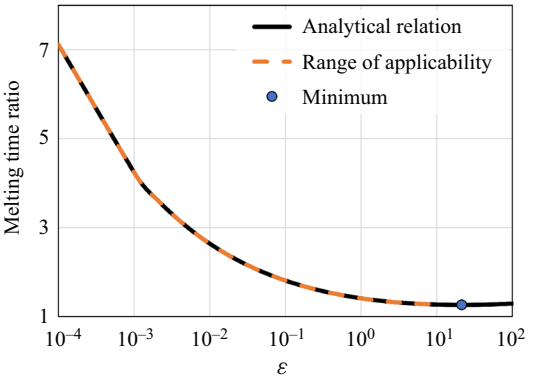

Figure 8. The melting time ratio between close-contact melting on superhydrophobic and regular surfaces as a function of ε, based on the approximate analytical model predictions: the analytical relation (6.9), the analytical model range of applicability (6.23), and the minimum point (6.13).

melting time, $Ste\,Fo_{melt}$, can be yielded by substituting $s_* = 1$ into (6.18):

$$\frac{Ste\,Fo_{melt}}{\lambda_* \rho_*} = \frac{3}{2}\left(\frac{3}{8}\varepsilon\right)^{1/3} + 1. \tag{6.19}$$

Finally, the dimensionless analysis results will be used to determine a criterion for the analytical model range of applicability. Both assumptions (1) and (2) of the analytical model can be rendered into dimensionless form to yield the condition

$$4\lambda_* \gg \delta_*. \tag{6.20}$$

Equation (6.16) can be substituted into (6.20) to yield the condition

$$4\lambda_* \gg \lambda_* \left(\frac{3}{8}\frac{\varepsilon}{1 - s_*}\right)^{1/3}, \tag{6.21}$$

The condition derived in (6.21) can be simplified into the form

$$\frac{8^3}{3}(1 - s_*) \gg \varepsilon. \tag{6.22}$$

It is clear that the condition stated in (6.22) can never hold in general, as for $s_* = 1$, it is always violated. However, for practical purposes, it is possible to assume that the analytical solution should provide sufficiently accurate results if 95 % of the melting process is captured correctly. Thus $s_* = 0.95$ is substituted into (6.22), formalizing the following condition:

$$8.5 \gg \varepsilon. \tag{6.23}$$

The condition in (6.23) indicates that for ε values sufficiently lower than 8.5, the approximate analytical model will replicate accurately the numerical model results. This result agrees with the analysis presented above as the cases $\phi = 0.16$, 0.08, 0.04, 0.02 and 0.01 correspond to ε values 26, 290, 574, 20, 0.8 and 0.04, respectively. Indeed, only the cases $\phi = 0.02$ and 0.01, where the criterion of (6.23) was satisfied, proved to capture accurately the numerical model results. This analysis is summarized in figure 8, where the melting time ratio as a function of ε, (6.9), is presented as well as the minimum point,

(6.13), and the approximate model applicability condition, (6.23). It is stressed that the minimum point (see (6.13)) does not satisfy the approximate model validity criterion (see (6.23)). Thus (6.13) captures the melting time increase trend only qualitatively but not quantitatively. Note that the non-monotonic trends observed above by the analytical model are associated with high ε values that lead to inaccurate and non-physical predictions of the numerical model results.

7. Stability of the liquid–gas interface

The previous sections dealt with the dynamics of close-contact melting on superhydrophobic surfaces. However, it is assumed implicitly that the liquid–gas interface remains stable, thus the Cassie state is maintained throughout the entire melting process. This is not an obvious assumption, as it is known that for sufficiently high pressure, the liquid–gas interface can collapse and transition into a Wenzel state (Fang *et al.* 2018). Many studies analysed the conditions for this transition to occur (Lobaton & Salamon 2007; Xue *et al.* 2012, 2016), as well as the liquid–gas interface longevity under unstable conditions (Emami *et al.* 2013; Hemeda & Tafreshi Vahedi 2014). The situation in the current problem is even more complex than other cases dealt with in the literature as the pressure in the thin molten layer depends on both space and time. Moreover, it is possible that the finite time that the liquid–gas interface takes to collapse is much larger than the melting time. Although it is possible to formulate a rather complicated and exact model that will take into account these effects, in the current work a much simpler approach is devised. It is possible to formulate a conservative condition that guarantees the liquid–gas interface stability under the assumption of worst scenario conditions. Accordingly, the maximum pressure, for both space and time, occurs at the cylinder's centre $r = 0$, at the beginning of the melting process $t = 0$. The maximum pressure p_{max} at the cylinder's centre can be derived by substituting $r = 0$ into (2.36):

$$p_{max} = p(r = 0) = \frac{3\mu R^2}{\delta^3}\frac{k}{\rho_s L}\frac{T_w - T_m}{\delta + \lambda_t}\frac{\delta + \lambda}{\delta + 4\lambda}. \tag{7.1}$$

Equation (7.1) can be substituted into (2.38) under the constraint $s(t = 0) = 0$, to derive a very simple relation for the maximum possible pressure for both space and time:

$$p_{max} = 2g\rho_s H. \tag{7.2}$$

It is therefore assumed that the pressure is constant and equal to p_{max}. The liquid–gas interface becomes unstable once the external pressure equals the capillary pressure (Lobaton & Salamon 2007). Thus the condition for the liquid–gas interface stability is

$$2g\rho_s H = -\frac{4\sigma\cos\theta}{D_{cap}^{eq}}, \tag{7.3}$$

where D_{cap}^{eq} is the equivalent pore diameter – defined by Hemeda & Tafreshi Vahedi (2014) for simplifying the interface stability analysis – σ is surface tension, and θ is the advancing contact angle. According to (7.3), a critical cylinder height can be defined that renders the

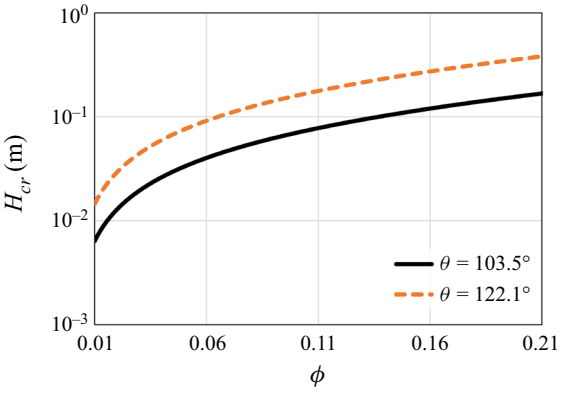

Figure 9. The critical cylinder's height for the liquid–gas interface stability as a function of the surface volume fraction ϕ; see (7.6). Two different advancing contact angles θ are examined.

liquid–gas interface unstable:

$$H_{cr} = -\frac{2\sigma\cos\theta}{D_{cap}^{eq} g\rho_s}. \tag{7.4}$$

For a superhydrophobic surface with an array of equidistant circular posts, the equivalent pore diameter can be defined as (see Hemeda & Tafreshi Vahedi 2014)

$$D_{cap}^{eq} = d\,\frac{1-\phi}{\phi}. \tag{7.5}$$

Equation (7.5) can be substituted into (7.4) to derive the following condition for the critical cylinder height:

$$H_{cr} = -\frac{2\sigma\cos\theta}{g\rho_s d}\,\frac{\phi}{1-\phi}. \tag{7.6}$$

Note that (7.6) provides a conservative estimate. Thus cylinder height values lower than H_{cr} must lead to a stable state. However, for higher height values, a more precise analysis is needed to determine whether or not the conditions lead to a stable state. The critical height predicted by (7.6) is presented in figure 9 as a function of ϕ. The surface conditions are chosen based on realistic superhydrophobic surfaces from the literature (see Lobaton & Salamon (2007)), using the same post diameter and material properties as in the analysis above. The value of σ is 72.8 mN m^{-1}. Two values of θ are examined, based on the measurements in Lobaton & Salamon (2007). Clearly, as the advancing contact angle increases, the liquid–gas interface stability is improved. It can be seen that for $\theta = 122.1°$, a cylinder's height of 1 cm, as used in the current study, should not lead to a collapse of the liquid–gas interface even for surface volume fractions ϕ as low as 0.01.

8. Conclusion

In the present study, the problem of close-contact melting of a vertical cylinder on a horizontal isothermal superhydrophobic surface has been analysed theoretically. A new numerical model has been derived, under several simplifying assumptions. The model can predict the melt fraction, molten layer thickness and heat transfer rate for a superhydrophobic surface with an array of equidistant circular posts. It is demonstrated

that under the limit of perfect slip and constant surface temperature, an analytical solution for the melting time can derived. This solution reveals that for any close-contact melting process of a vertical cylinder on a horizontal isothermal superhydrophobic surface, the possible melting time enhancement, in comparison with a regular no-slip surface, cannot exceed 30 %. Numerical solution of the model governing equations, for a representative case of an ice cylinder, shows that for relatively high surface volume fractions, $\phi > 0.04$, the effect of the superhydrophobic surface on the melting rate, molten layer thickness and heat transfer rate is negligible. However, for lower ϕ values, the close-contact melting process on a superhydrophobic surface can be roughly two times longer than the case for a regular surface. The analysis shows that although the thin molten layer thickness is decreased, the overall heat transfer rate is decreased due to the thermal slip effect, which proves dominant.

An approximate analytical model is developed for gaining fundamental understanding of the problem dynamics and fast estimations. The new analytical model predictions are compared extensively against the numerical model results. For low ϕ values, the analytical model provides excellent agreement with the numerical model results. For high ϕ values, the analytical model overpredicts the melting time and the molten layer thickness, and underpredicts the heat transfer rate. Also, the analytical model can reproduce the correct physical trend for the molten layer thickness as ϕ is varied. On the other hand, the trends, as ϕ is varied, for the melt fraction and heat transfer rate do not agree with the numerical model results. Dimensional analysis reveals that according to the analytical model predictions, the ratio between the melting times for superhydrophobic and regular surfaces is governed by a single dimensionless group, $\varepsilon = Ste\, R_*^2/Ga\, Pr\, \rho_*^2 \lambda_*^4$. It is also proved that according to the analytical model predictions, the melting time on a superhydrophobic surface is always longer by more than 26 % in comparison with a regular surface. This result agrees qualitatively with the numerical model predictions that show that the melting time on a superhydrophobic surface is always longer than on a regular surface. Based on this analysis, it is shown that for $\varepsilon \ll 8.5$, the analytical model provides an excellent estimate of the numerical model results. Finally, a conservative criterion for the liquid–gas interface stability is derived. It is demonstrated that the Cassie state can be maintained throughout the entire close-contact melting process for all the cases studied in the current work. It is stressed that the current model provides, for the first time, quantitative predictions for the phenomenon of close-contact melting on superhydrophobic surfaces. Thus in the future, the model limitations should be assessed carefully against high-fidelity simulations and experimental results. Moreover, the role of metastability will be explored in detail; see, for instance, (Poole *et al.* 1992; Palmer *et al.* 2014; Magaletti, Gallo & Casciola 2021). Future work will deal with the close-contact melting dynamics of additional surface micro-textures and simple geometric configurations. Also, the liquid–gas interface longevity under close-contact melting conditions will be studied in detail.

Acknowledgements. The author would like to thank Prof G. Ziskind of Ben-Gurion University of the Negev for introducing him to the field of solid–liquid phase change and many helpful discussions throughout the years.

Funding. This research received no specific grant from any funding agency, or commercial or not-for-profit sectors.

Declaration of interests. The author reports no conflict of interest.

Author ORCIDs.
Yoram Kozak https://orcid.org/0000-0001-8542-8257.

References

Alexiades, V. & Solomon, A.D. 2018 *Mathematical Modeling of Melting and Freezing Processes*. Routledge.

Aljaghtham, M., Premnath, K. & Alsulami, R. 2021 Investigation of time-dependent microscale close contact melting. *Intl J. Heat Mass Transfer* **166**, 120742.

Bahrami, P.A. & Wang, T.G. 1987 Analysis of gravity and conduction-driven melting in a sphere. *ASME J. Heat Transfer* **109** (3), 806–809.

Bareiss, M. & Beer, H. 1984 An analytical solution of the heat transfer process during melting of an unfixed solid phase change material inside a horizontal tube. *Intl J. Heat Mass Transfer* **27** (5), 739–746.

Bejan, A. 1992 Single correlation for theoretical contact melting results in various geometries. *Intl Commun. Heat Mass Transfer* **19** (4), 473–483.

Bejan, A. 1994 Contact melting heat transfer and lubrication. In *Advances in Heat Transfer* (ed. J.P. Hartnett, T.F. Irvine Jr & Y.I. Cho). Elsevier.

Betzel, T. & Beer, H. 1988 Solidification and melting heat transfer to an unfixed phase change material (PCM) encapsulated in a horizontal concentric annulus. *Wärme-Stoffübertrag.* **22** (6), 335–344.

Chen, L., Guo, Z. & Liu, W. 2017 Outmatching superhydrophobicity: bio-inspired re-entrant curvature for mighty superamphiphobicity in air. *J. Mater. Chem.* A **5** (28), 14480–14507.

Chen, W., Cheng, S., Luo, Z. & Gu, W. 1993 Study of contact melting inside isothermally heated vertical cylindrical capsules. *J. Therm. Sci.* **2** (3), 190–195.

Cregan, V., Williams, J. & Myers, T.G. 2020 Contact melting of a rectangular block with temperature-dependent properties. *Intl J. Therm. Sci.* **150**, 106218.

Davis, A.M.J. & Lauga, E. 2010 Hydrodynamic friction of fakir-like superhydrophobic surfaces. *J. Fluid Mech.* **661**, 402–411.

Emami, B., Hemeda, A.A., Amrei, M.M., Luzar, A., Gad-el Hak, M. & Vahedi Tafreshi, H. 2013 Predicting longevity of submerged superhydrophobic surfaces with parallel grooves. *Phys. Fluids* **25** (6), 062108.

Emerman, S.H. & Turcotte, D.L. 1983 Stokes's problem with melting. *Intl J. Heat Mass Transfer* **26** (11), 1625–1630.

Enright, R., Hodes, M., Salamon, T. & Muzychka, Y. 2014 Isoflux Nusselt number and slip length formulae for superhydrophobic microchannels. *ASME J. Heat Transfer* **136** (1), 012402.

Faden, M., König-Haagen, A., Höhlein, S. & Brüggemann, D. 2018 An implicit algorithm for melting and settling of phase change material inside macrocapsules. *Intl J. Heat Mass Transfer* **117**, 757–767.

Fang, W., Guo, H.Y., Li, B., Li, Q. & Feng, X.Q. 2018 Revisiting the critical condition for the Cassie–Wenzel transition on micropillar-structured surfaces. *Langmuir* **34** (13), 3838–3844.

Fomin, S.A., Wilchinsky, A.V. & Saitoh, T.S. 2000 Close-contact melting inside an elliptical cylinder. *J. Sol. Energy Engng* **122** (4), 192–195.

Groulx, D. & Lacroix, M. 2003 Effects of convection and inertia on close contact melting. *Intl J. Therm. Sci.* **42** (12), 1073–1080.

Groulx, D. & Lacroix, M. 2006 Study of close contact melting of ice from a sliding heated flat plate. *Intl J. Heat Mass Transfer* **49** (23-24), 4407–4416.

Groulx, D. & Lacroix, M. 2007 Study of the effect of convection on close contact melting of high Prandtl number substances. *Intl J. Therm. Sci.* **46** (3), 213–220.

Gudibande, N. & Iyer, K. 2017 Numerical simulation of contact melting using the cell-splitting modified enthalpy method. *Numer. Heat Transfer* B **71** (1), 84–107.

Hejazi, V., Sobolev, K. & Nosonovsky, M. 2013 From superhydrophobicity to icephobicity: forces and interaction analysis. *Sci. Rep.* **3** (1), 2194.

Hemeda, A.A. & Tafreshi Vahedi, H. 2014 General formulations for predicting longevity of submerged superhydrophobic surfaces composed of pores or posts. *Langmuir* **30** (34), 10317–10327.

Hirata, T., Makino, Y. & Kaneko, Y. 1991 Analysis of close-contact melting for octadecane and ice inside isothermally heated horizontal rectangular capsule. *Intl J. Heat Mass Transfer* **34** (12), 3097–3106.

Hu, N., Zhu, Z.Q., Li, Z.R., Tu, J. & Fan, L.W. 2018 Close-contact melting heat transfer on a heated horizontal plate: revisited in the presence of nano-enhanced phase change materials (NEPCM). *Intl J. Heat Mass Transfer* **124**, 794–799.

Kasibhatla, R.R. & Brüggemann, D. 2021 Coupled conjugate heat transfer model for melting of PCM in cylindrical capsules. *Appl. Therm. Engng* **184**, 116301.

Kasibhatla, R.R., König-Haagen, A., Rösler, F. & Brüggemann, D. 2017 Numerical modelling of melting and settling of an encapsulated PCM using variable viscosity. *Heat Mass Transfer* **53** (5), 1735–1744.

KOZAK, Y., ROZENFELD, T. & ZISKIND, G. 2014 Close-contact melting in vertical annular enclosures with a non-isothermal base: theoretical modeling and application to thermal storage. *Intl J. Heat Mass Transfer* **72**, 114–127.

KOZAK, Y., ZENG, Y., AL GHOSSEIN, R.M., KHODADADI, J.M. & ZISKIND, G. 2019 Close-contact melting on an isothermal surface with the inclusion of non-Newtonian effects. *J. Fluid Mech.* **865**, 720–742.

KOZAK, Y. & ZISKIND, G. 2017 Novel enthalpy method for modeling of PCM melting accompanied by sinking of the solid phase. *Intl J. Heat Mass Transfer* **112**, 568–586.

LAFUMA, A. & QUÉRÉ, D. 2003 Superhydrophobic states. *Nat. Mater.* **2** (7), 457–460.

LAUGA, E. & STONE, H.A. 2003 Effective slip in pressure-driven Stokes flow. *J. Fluid Mech.* **489**, 55–77.

LEA, J.F. & STEGALL, R.D. 1973 A two-dimensional theory of temperature and pressure effects on ice melting rates with a heated plate. *Trans. ASME J. Heat Transfer* **95** (4), 571–573.

LEE, C., CHOI, C.H. & KIM, C.J. 2016 Superhydrophobic drag reduction in laminar flows: a critical review. *Exp. Fluids* **57** (12), 176.

LIRAVI, M., PAKZAD, H., MOOSAVI, A. & NOURI-BORUJERDI, A. 2020 A comprehensive review on recent advances in superhydrophobic surfaces and their applications for drag reduction. *Prog. Org. Coat.* **140**, 105537.

LOBATON, E.J. & SALAMON, T.R. 2007 Computation of constant mean curvature surfaces: application to the gas–liquid interface of a pressurized fluid on a superhydrophobic surface. *J. Colloid Interface Sci.* **314** (1), 184–198.

LV, P., XUE, Y., SHI, Y., LIN, H. & DUAN, H. 2014 Metastable states and wetting transition of submerged superhydrophobic structures. *Phys. Rev. Lett.* **112** (19), 196101.

MAGALETTI, F., GALLO, M. & CASCIOLA, C.M. 2021 Water cavitation from ambient to high temperatures. *Sci. Rep.* **11** (1), 1–10.

MILJKOVIC, N., ENRIGHT, R. & WANG, E.N. 2013 Modeling and optimization of superhydrophobic condensation. *Trans. ASME J. Heat Transfer* **135** (11), 111004.

MOALLEMI, M.K. & VISKANTA, R. 1986 Analysis of close-contact melting heat transfer. *Intl J. Heat Mass Transfer* **29** (6), 855–867.

MOALLEMI, M.K., WEBB, B.W. & VISKANTA, R. 1986 An experimental and analytical study of close-contact melting. *Trans. ASME J. Heat Transfer* **108** (4), 894–899.

MOORE, F.E. & BAYAZITOGLU, Y. 1982 Melting within a spherical enclosure. *Trans. ASME J. Heat Transfer* **104** (1), 19–23.

MYERS, T.G., MITCHELL, S.L. & MUCHATIBAYA, G. 2008 Unsteady contact melting of a rectangular cross-section material on a flat plate. *Phys. Fluids* **20** (10), 103101.

OCKENDON, H. & OCKENDON, J.R. 1995 *Viscous Flow*. Cambridge University Press.

OU, J., PEROT, B. & ROTHSTEIN, J.P. 2004 Laminar drag reduction in microchannels using ultrahydrophobic surfaces. *Phys. Fluids* **16** (12), 4635–4643.

PALMER, J.C., MARTELLI, F., LIU, Y., CAR, R., PANAGIOTOPOULOS, A.Z. & DEBENEDETTI, P.G. 2014 Metastable liquid–liquid transition in a molecular model of water. *Nature* **510** (7505), 385–388.

PAN, C., CHARLES, J., VERMAAK, N., ROMERO, C., NETI, S., ZHENG, Y., CHEN, C.H. & BONNER III, R. 2018 Experimental, numerical and analytic study of unconstrained melting in a vertical cylinder with a focus on mushy region effects. *Intl J. Heat Mass Transfer* **124**, 1015–1024.

PAPADOPOULOS, P., MAMMEN, L., DENG, X., VOLLMER, D. & BUTT, H.J. 2013 How superhydrophobicity breaks down. *Proc. Natl Acad. Sci. USA* **110** (9), 3254–3258.

PARK, U.J., KANG, K., LEE, H.J., JEONG, C.H., PARK, J.Y. & LEE, S.H. 2021 Numerical analysis of the close-contact heat transfer of the electro-thermal drilling probes for glacier-ice exploration. *J. Mech. Sci. Technol.* **35** (3), 1309–1317.

PATANKAR, N.A. 2010 Consolidation of hydrophobic transition criteria by using an approximate energy minimization approach. *Langmuir* **26** (11), 8941–8945.

POOLE, P.H., SCIORTINO, F., ESSMANN, U. & STANLEY, H.E. 1992 Phase behaviour of metastable water. *Nature* **360** (6402), 324–328.

QUÉRÉ, D. 2008 Wetting and roughness. *Annu. Rev. Mater. Res.* **38**, 71–99.

ROTHSTEIN, J.P. 2010 Slip on superhydrophobic surfaces. *Annu. Rev. Fluid Mech.* **42**, 89–109.

SAITO, A., HONG, H. & HIROKANE, O. 1992 Heat transfer enhancement in the direct contact melting process. *Intl J. Heat Mass Transfer* **35** (2), 295–305.

SAITO, A., UTAKA, Y., AKIYOSHI, M. & KATAYAMA, K. 1985*a* On the contact heat transfer with melting: 1st report: experimental study. *Bull. JSME* **28** (240), 1142–1149.

SAITO, A., UTAKA, Y., AKIYOSHI, M. & KATAYAMA, K. 1985*b* On the contact heat transfer with melting: 2nd report: analytical study. *Bull. JSME* **28** (242), 1703–1709.

SAITO, A., UTAKA, Y., SHINODA, K. & KATAYAMA, K. 1986 Basic research on the latent heat thermal energy storage utilizing the contact melting phenomena. *Bull. JSME* **29** (255), 2946–2952.

SCHÜLLER, K. & KOWALSKI, J. 2017 Spatially varying heat flux driven close-contact melting – a Lagrangian approach. *Intl J. Heat Mass Transfer* **115**, 1276–1287.

SHAO, Z., WANG, Y. & BAI, H. 2020 A superhydrophobic textile inspired by polar bear hair for both in air and underwater thermal insulation. *Chem. Engng J.* **397**, 125441.

SHOCKNER, T. & ZISKIND, G. 2021 Combined close-contact and convective melting in a vertical cylindrical enclosure. *Intl J. Heat Mass Transfer* **177**, 121492.

SHREVE, R.L. 1962 Theory of performance of isothermal solid-nose hotpoints boring in temperate ice. *J. Glaciol.* **4** (32), 151–160.

SNOEIJER, J.H & ANDREOTTI, B. 2013 Moving contact lines: scales, regimes, and dynamical transitions. *Annu. Rev. Fluid Mech.* **45**, 269–292.

SPARROW, E.M. & GEIGER, G.T. 1986 Melting in a horizontal tube with the solid either constrained or free to fall under gravity. *Intl J. Heat Mass Transfer* **29** (7), 1007–1019.

STEIGERWALT LAM, L., MELNICK, C., HODES, M., ZISKIND, G. & ENRIGHT, R. 2014 Nusselt numbers for thermally developing Couette flow with hydrodynamic and thermal slip. *Trans. ASME J. Heat Transfer* **136** (5), 051703.

TURKYILMAZOGLU, M. 2019 Direct contact melting due to a permeable rotating disk. *Phys. Fluids* **31** (2), 023603.

WILSON, W.R.D. 1976 Lubrication by a melting solid. *Trans. ASME J. Lubr. Technol.* **98** (1), 22–26.

XUE, Y., CHU, S., LV, P. & DUAN, H. 2012 Importance of hierarchical structures in wetting stability on submersed superhydrophobic surfaces. *Langmuir* **28** (25), 9440–9450.

XUE, Y., LV, P., LIN, H. & DUAN, H. 2016 Underwater superhydrophobicity: stability, design and regulation, and applications. *Appl. Mech. Rev.* **68** (3), 030803.

YBERT, C., BARENTIN, C., COTTIN-BIZONNE, C., JOSEPH, P. & BOCQUET, L. 2007 Achieving large slip with superhydrophobic surfaces: scaling laws for generic geometries. *Phys. Fluids* **19** (12), 123601.

YOO, H., HONG, H. & KIM, C.J. 1998 Effects of transverse convection and solid–liquid density difference on the steady close-contact melting. *Intl J. Heat Fluid Flow* **19** (4), 368–373.

ZHENG, Q.S., YU, Y. & ZHAO, Z.H. 2005 Effects of hydraulic pressure on the stability and transition of wetting modes of superhydrophobic surfaces. *Langmuir* **21** (26), 12207–12212.

ZISKIND, G. & KOZAK, Y. 2018 *Encyclopedia of Thermal Packaging: Set 3: Thermal Packaging Applications Volume 3: Phase Change Materials for Thermal Management of Electronic Components*. World Scientific.